

Particle segregation using crystal-like structure of capsules in wall-bounded shear flow

Shunichi Ishida,¹ Ryota Matsumoto,¹ Daiki Matsunaga,^{2,*} and Yohsuke Imai^{1,†}

¹Graduate School of Engineering, Kobe University, Kobe 6578501, Japan

²Graduate School of Engineering Science, Osaka University, Toyonaka 5608531, Japan



(Received 6 September 2021; accepted 24 May 2022; published 10 June 2022)

In a wall-bounded shear flow, deformable particles form a crystal-like structure [Phys. Rev. Lett. **120**, 268102 (2018)]. To expand the applicability of microfluidic devices to particle sorting, we performed a lattice Boltzmann simulation. In this study, the crystal structure of capsules can be utilized to segregate capsules of different sizes. We add small capsules into a system where large capsules form a crystal structure, and find that the movement of the small capsules changes significantly with size ratio R_a . When the sizes of the small capsules were comparable to those of the large capsules ($R_a \sim 1$), the small capsules are trapped in the crystal structure. In addition, they composed the crystal with the large capsules and traveled in a diffusive manner. However, when $R_a \sim 0.6$ or lower, the small capsules were depleted from the crystal layer due to the low lift velocity, and they continuously traveled in an advective manner. Furthermore, we found that the stiffness of the small capsules had only a slight influence on this phenomenon. The results suggest that the crystal structure of capsules can be used to trap capsules of comparable sizes or to exclude capsules of smaller sizes. The findings of this study can serve as practical basis for microfluidic applications for segregating and sorting different types of soft particles.

DOI: [10.1103/PhysRevFluids.7.063601](https://doi.org/10.1103/PhysRevFluids.7.063601)

I. INTRODUCTION

Segregating different types of cells is one of the fundamental tasks for microfluidic devices [1]. In previous studies, the segregation of different particles or cells was achieved in microfluidic devices using inertial migration [2–4], dean flow [5,6], and magnetic fields [7,8]. These technologies have been widely used in the biomedical fields to collect rare cells from the blood, such as leukocytes [9,10], platelets [11,12], and circulating tumor cells [9,13–15]. In this study, we developed an alternative approach for particle segregation based on the crystal-like structure of deformable particles.

Shen *et al.* [16] recently revealed that red blood cells, or other deformable particles, such as capsules and vesicles, form crystal-like self-organized patterns in a wall-bounded shear flow. The patterns significantly change with the volume fraction of the cells; with an increase in volume fraction, the cell formation transforms from a chainlike structure [17,18] to a crystal-like structure, and finally to a disordered state. Due to the effect of two parallel plates [19,20], the cells first migrate towards the channel center and remain at the midplane of the channel. Because of the quadrupolar flow field generated by each cell [16,18], the cells attempt to align in the flow direction, while exhibiting cell-cell repulsion in the vorticity direction. They gradually form a chain or crystal-like structure, depending on the volume fraction of the cells. Moreover, a discussion was presented on

*daiki.matsunaga.es@osaka-u.ac.jp

†yimai@mech.kobe-u.ac.jp

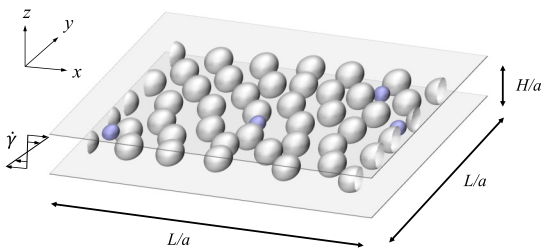


FIG. 1. Two types of capsules, type A (gray) and type B (blue), are suspended in a fluid between two parallel plates, where $R_a = 0.6$.

the mechanism underlying the equilibrium particle-particle distances in the self-organized patterns. By considering the interplay of the background shear and the hydrodynamic interaction between two particles, a theory for the equilibrium distance of the particles was proposed.

In a previous study [16], the mechanism of the emergent dynamics of the crystal structure of deformable particles in a wall-bounded shear flow was clarified. When small particles are added to the crystal structure, their behaviors may vary depending on their size.

In this study, we hypothesize that this crystal structure can be utilized to segregate two different types of capsules. To segregate two capsule types (type A and type B) under shear flow, it is essential to realize a significant difference in the advected distance. If type-A capsules could be made to stay approximately near the initial position, whereas type-B capsules are continuously advected downstream and washed away from the channel, the system can be utilized to segregate deformable particles of different properties. We tested this hypothesis using a lattice Boltzmann simulation of capsules in a wall-bounded shear flow. We first analyzed the interaction between two capsules of different sizes using the theory proposed by Shen *et al.* [16]. We then examined the behavior of the small capsules in a wall-bounded shear flow and present a discussion of the effect of the stiffness of the small capsules on this problem.

II. PROBLEM STATEMENT AND METHODS

Figure 1 presents a schematic of this study. Two types of spherical capsules were considered, namely, types A and B, suspended in a fluid between two parallel plates with width H . Both types of capsules were neutrally buoyant, and their inner fluids exhibited the same viscosity as the outer fluid. Type-A and type-B capsules had radii a_A and a_B and surface shear elastic moduli G_A and G_B [21]. The domain size was $L \times L \times H = 20a_A \times 20a_A \times 3a_A$, and a shear flow with shear rate $\dot{\gamma}$ was applied to the domain under periodic boundary conditions in the x and y directions.

A constitutive law proposed by Skalak *et al.* [22] was used to model the membrane of capsules. In particular, the strain energy function is expressed as follows:

$$w_{A,B} = \frac{G_{A,B}}{4} (I_1^2 + 2I_1 - 2I_2 + CI_2^2), \quad (1)$$

where $C = 100$ is the area dilation constant, $I_1 = \lambda_1^2 + \lambda_2^2 - 2$, $I_2 = \lambda_1^2 \lambda_2^2$, and λ_1 and λ_2 are principal extension ratios. Membrane mechanics are expressed by the following equilibrium equation:

$$\int_S \hat{\mathbf{u}} \cdot \mathbf{q} dS = \int_S \hat{\boldsymbol{\varepsilon}} : \mathbf{T} dS, \quad (2)$$

where \mathbf{T} denotes the Cauchy stress tensor, \mathbf{q} denotes the load on the membrane, $\hat{\mathbf{u}}$ denotes the virtual displacement, and $\hat{\boldsymbol{\varepsilon}}$ denotes the virtual strain. The capsule membrane was discretized into 5120 triangular meshes, and the finite element method (FEM) was used to solve membrane mechanics [23]. Moreover, the bending resistance was considered [24].

The fluid mechanics were solved using the lattice Boltzmann method (LBM) [25]:

$$f_i(\mathbf{x} + \mathbf{c}_i \Delta t, t + \Delta t) = f_i(\mathbf{x}, t) - \frac{1}{\tau} [f_i(\mathbf{x}, t) - f_i^{eq}(\mathbf{x}, t)] + \left(1 - \frac{1}{2\tau}\right) \omega_i \left(\frac{\mathbf{c}_i - \mathbf{u}}{c_s^2} + \frac{\mathbf{c}_i \cdot \mathbf{u}}{c_s^4} \right) \cdot \mathbf{F}(\mathbf{x}, t), \quad (3)$$

where f_i is the density distribution function for the direction i , \mathbf{c}_i is the discrete direction vector, Δt is the time interval, τ is the relaxation time, f_i^{eq} is the equilibrium distribution function, ω_i is the weight coefficient, \mathbf{u} is the fluid velocity, c_s is the speed of sound, and \mathbf{F} is the force term. The incompressible Navier-Stokes equation is recovered from Eq. (3) using the Chapman-Enskog expansion [26]. The FEM and LBM are coupled using the immersed boundary method [27]. The force $\mathbf{F}(\mathbf{x})$ at the fluid node \mathbf{x} is calculated as follows:

$$\mathbf{F}(\mathbf{x}, t) = \sum \mathcal{D}(\mathbf{x} - \mathbf{X}) \mathbf{F}(\mathbf{X}, t), \quad (4)$$

where \mathbf{X} is the position of the membrane node, and $\mathcal{D}(\mathbf{x})$ is the smoothed delta function. Similarly, the velocity at the membrane node $\mathbf{u}(\mathbf{X})$ is interpolated from the surrounding fluid node as follows:

$$\mathbf{u}(\mathbf{X}, t) = \sum \mathcal{D}(\mathbf{x} - \mathbf{X}) \mathbf{u}(\mathbf{x}, t). \quad (5)$$

A volume constraint [28] was applied to each capsule to maintain a nearly constant inner volume in this study.

We fixed the Reynolds number of the type-A capsule at $\text{Re}_A = \rho \dot{\gamma} a_A^2 / \mu = 0.1$ and the capillary number at $\text{Ca}_A = \mu \dot{\gamma} a_A / G_A = 0.1$, where μ is the fluid viscosity, and ρ is the fluid density. The volume fraction and area fraction of type-A capsules $\phi = 4\pi a_A^3 N_A / (3L^2 H)$ and $\phi_{2D} = \pi a_A^2 N_A / L^2$ were set to 0.14 and 0.32, respectively, where $N_A = 41$ is the number of type-A capsules. To characterize the capsule size and deformability, we defined the size ratio $R_a = a_B / a_A$ and the capillary number ratio $R_{Ca} = \frac{\mu \dot{\gamma} a_B / G_B}{\mu \dot{\gamma} a_A / G_A} = a_B G_A / a_A G_B$ [21].

A grid size of $\Delta x = a_A / 16$ was utilized (the effect of the grid size is checked in Appendix A), and graphics processing unit (GPU) parallelization (NVIDIA Tesla A100) was used to accelerate the computation. The proposed method was validated by conducting various test problems, including the deformation of spherical cells and healthy red blood cells (RBCs) in shear flow and the thickness of the cell-depleted peripheral layer in channel flow [29]. In previous studies, we successfully applied this method to the simulation of margination and adhesion of leukocytes, circulating tumor cells, and malaria-infected RBCs [30–32].

III. RESULTS AND DISCUSSION

A. Theory: Interaction between large and small capsules

When two identical capsules have an intercapsule distance ℓ_x and $2\ell_z$ [Fig. 2(a)], there is a stable fixed point due to the hydrodynamic interaction between capsules, as demonstrated by Shen *et al.* [16]. To better understand the influence of the capsule size on the equilibrium process, we can extend their theory to the problem addressed in this study.

Consider two capsules (types A and B) located alongside each other as shown in Fig. 2(a), where $a_B \leq a_A$. In this subsection, we assume that the capsules are in the same y plane, and focus only on the two-dimensional velocity of the type-B capsule, i.e., $\mathbf{u}^B = (u_x^B, u_z^B)$. The x -directional velocity u_x^B consists of two velocities: the velocity due to the hydrodynamic interaction between the type-A and -B capsules u_x^Q and the background shear flow u_x^{SSF} . Due to the quadrupole flow field generated by the type-A capsule, the type-B capsule undergoes an x -directional flow as follows:

$$u_x^Q \sim \frac{\Sigma_A H}{\mu \ell_x^3} \sim -\frac{\dot{\gamma} a_A^3 H}{\ell_x^3}, \quad (6)$$

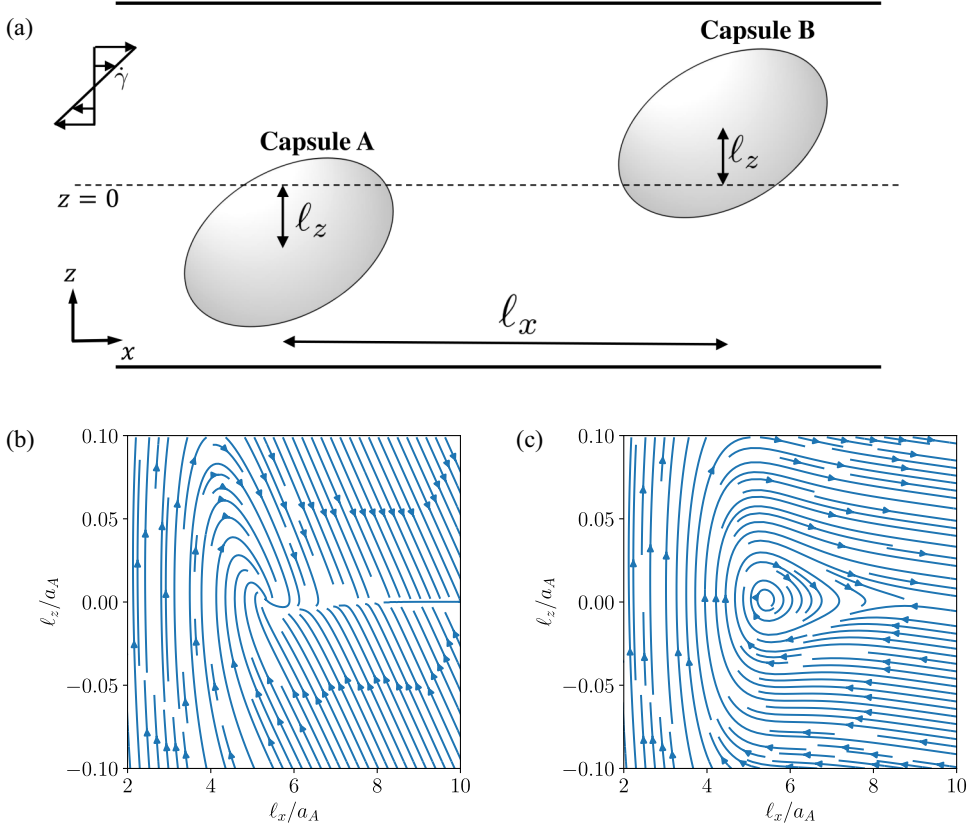


FIG. 2. (a) A schematic showing two capsules reaching a stable distance due to the hydrodynamic effects. Dashed line denotes the channel center. (b) Trajectory of distance between two capsules (relative position of the capsules) (ℓ_x, ℓ_z) for (b) $R_a = 1.0$ and (c) $R_a = 0.4$. Note that Eqs. (7) and (10) with prefactors $C_1 = 0.08$, $C_2 = 15.0$, $C_3 = 1.5$ ($Ca = 0.1$) and conditions $R_{Ca} = 1.0$ and $H/a_A = 3.0$ are utilized.

where $\Sigma_A \sim -\dot{\gamma}\mu a_A^3$ is a variable with the same dimension as the stresslet, and the superscript Q represents the hydrodynamic interaction. Given that the background shear flow transports the type-B capsule with velocity $u_x^{\text{SSF}} = \dot{\gamma}\ell_z$, the net x -directional velocity of type B is as follows:

$$\frac{u_x^B}{\dot{\gamma}a_A} = \frac{u_x^Q + u_x^{\text{SSF}}}{\dot{\gamma}a_A} = -C_1 \left(\frac{a_A}{\ell_x} \right)^3 \cdot \frac{H}{a_A} + \frac{\ell_z}{a_A}, \quad (7)$$

where C_1 is a numerical prefactor of order 1 [16]. The z -directional velocity u_z^B consists of two velocities: the velocity of the wall-induced migration u_z^{lift} , and that of the hydrodynamic interaction u_z^Q . The velocity of the wall-induced migration [19] scales with

$$u_z^{\text{lift}} \sim \frac{\Sigma_B \ell_z}{\mu H^3} \sim -\dot{\gamma}\ell_z \left(\frac{a_B}{H} \right)^3, \quad (8)$$

where $\Sigma_B \sim -\dot{\gamma}\mu a_B^3$, whereas that of the hydrodynamic interaction is expressed as follows:

$$u_z^Q \sim -\frac{\Sigma_A}{\mu H^2} \sqrt{\frac{\ell_x}{H}} \exp\left(-\frac{b_2 \ell_x}{H}\right) \cos\left(\frac{b_1 \ell_x}{H} - b_3\right), \quad (9)$$

where $b_1 \sim 2.25$, $b_2 \sim 4.21$ and $b_3 \sim 2.49$ [16]. The net z -directional velocity of type B is expressed as follows:

$$\frac{u_z^B}{\dot{\gamma}a_A} = \frac{u_z^{\text{lift}} + u_z^Q}{\dot{\gamma}a_A} = \left(\frac{a_A}{H}\right)^3 \left[-C_3 R_a^3 \frac{\ell_z}{a_A} + C_2 \frac{H}{a_A} \sqrt{\frac{\ell_x}{H}} \exp\left(-\frac{b_2 \ell_x}{H}\right) \cos\left(\frac{b_1 \ell_x}{H} - b_3\right) \right], \quad (10)$$

where C_2 and $C_3 \sim 1$ are the numerical prefactors. The previous study [16] obtained the fixed point as $u_x^B = u_z^B = 0$.

Figure 2(b) presents the capsule trajectory for various intercapsule distances (ℓ_x, ℓ_z) . The two capsules were assumed to be identical ($R_a = 1$, $R_{Ca} = 1$), and prefactors $C_1 = 0.08$, $C_2 = 15.0$ and $C_3 = 1.5$ were considered, which were estimated by fitting the velocity curve of a simulation of two capsules approaching the stable distance ($Ca = 0.1$). Under these conditions, the capsules were situated at a stable fixed point around $(\ell_x/a_A, \ell_z/a_A) = (5.5, 0.0)$, as predicted in a previous study [16]. The capsules reached the stable fixed point from a wide range of initial positions. Moreover, they were then maintained at the same height ($\ell_z \sim 0$) and formed a crystal with the other capsules.

When the size of the type-B capsule decreases to $R_a = 0.4$, the capsule trajectory changed significantly, as shown in Fig. 2(c). Note that only parameter R_a in Eq. (10) was changed. Although prefactors C_1 , C_2 , and C_3 depend on R_a (in addition to Ca and R_{Ca}), this dependency was ignored for simplicity. Compared with the case of $R_a = 1$ [Fig. 2(b)], the type-B capsule has a narrower range of initial positions to reach the stable point, and the capsules are likely to be carried away by shear flow from a wide range of initial positions. This difference can be attributed to the lift velocity, which is significantly dependent on the capsule size $u^{\text{lift}} \propto (a/H)^{-3}$. When the capsule size decreased, the lift velocity from the image system decreased rapidly, and the capsule required a longer time to focus on the center plane, where $z/H \sim 0$. Due to the increase in the focusing time, the type-B capsule has a narrow range of initial positions to reach the stable capsule-capsule distance, and it is likely to be carried by the flow in the x direction. The stability analysis (Appendix C) also suggests that the stability of the fixed point decreases as R_a decreases.

In summary, the two capsules stabilized at a distance when their sizes were highly similar. When a capsule is small compared to another capsule, it has a narrow range of initial positions to stabilize due to the low lift velocity. This simple toy model suggests that it is difficult for small capsules to migrate to the center plane in a wall-bounded shear flow. Therefore it cannot form a crystal-like structure with large capsules.

B. Simulation: Small capsules in the crystal structure

Subsequently, we studied the behavior of small capsules in a wall-bounded shear flow based on numerical simulations. We confirmed that type-A capsules form a crystal structure as reported in a previous study [16]. In the steady state, all the capsules were located near the midplane of the channel ($z/a_A = 0$), with the condition that the capsules were subject to lift velocity [7,8,16,19], detailed in the previous section. The following values were used for all the simulations in this study: $H/a_A = 3.0$, $L/a_A = 20.0$, $\phi = 0.14$, $\phi_{2D} = 0.32$, and $Ca_A = 0.1$.

We then added type-B capsules to this system and examined seven cases of R_a in the range 0.4–1.0, with R_{Ca} fixed at 1.0. Figure 3 reveals that the movement of type-B capsules changed significantly for R_a (see Movies 1 and 2 in the Supplemental Material [33]). When the size of the type-B capsules was comparable to that of type-A capsules ($R_a = 1.0$), the type-B capsules formed a crystal-like pattern with the type-A capsules [Fig. 3(a)]. This is because type-B capsules were identical to the type-A capsules under those conditions ($R_{Ca} = 1.0$ and $R_a = 1.0$). When the type-B capsules were smaller than the type-A capsules ($R_a = 0.4$ [Fig. 3(b)]), type-B capsules were depleted from the crystal and did not remain in the same plane as the type-A capsules ($z/a_A \sim 0$). Instead of forming a crystal-like pattern with type-A capsules, the type-B capsules continuously traveled between or outside the crystal in an advective manner.

To characterize the capsule motions, the mean square displacements (MSDs) were calculated, as shown in Fig. 4. Regardless of R_a , the MSD of the type-A capsules was nearly constant [Fig. 4(b)]

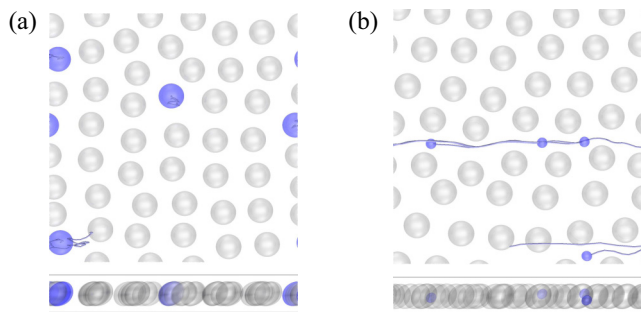


FIG. 3. Snapshots showing the type-B capsule movements through crystal-like pattern of type-A capsules for (a) $R_a = 1.0$ and (b) $R_a = 0.4$. The four type-B capsules and their trajectories are shown in blue, while type-A capsules are shown in gray. Top figures are views of the xy plane, while bottom figures are the xz plane (side view). $R_{Ca} = 1.0$ and $Ca_A = 0.1$.

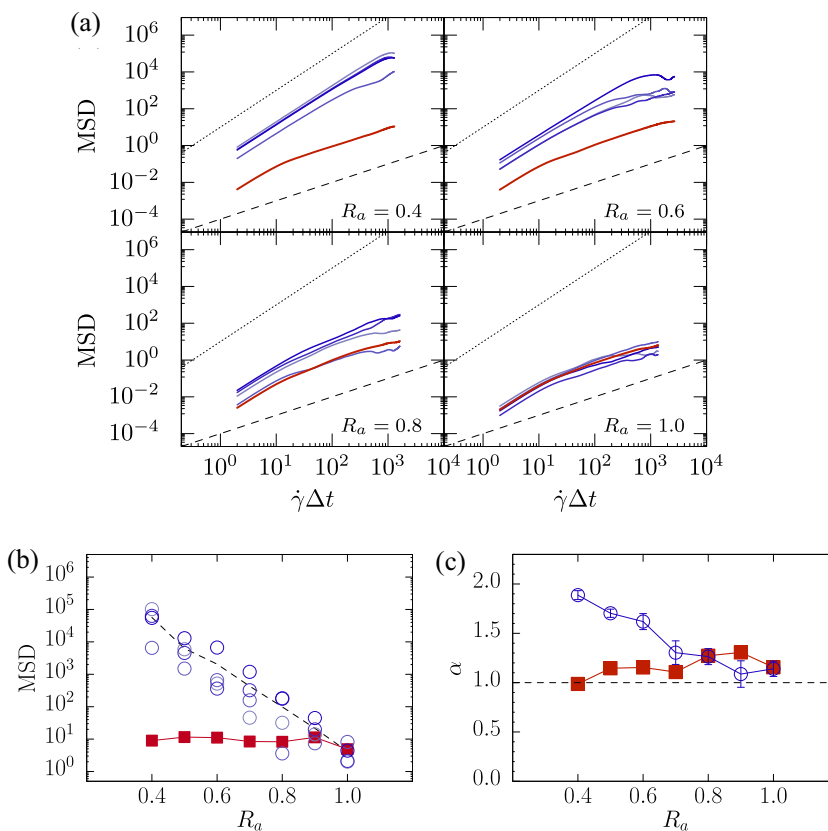


FIG. 4. (a) Mean square displacements (MSDs) of type-A (red line) and -B (blue lines) capsules for different R_a and $R_{Ca} = 1.0$. The red line shows the average MSD of type-A capsules, while each blue line shows MSD of each type-B capsule. Dashed lines show the scaling $\alpha = 1$ (diffusive), while dotted lines show the scaling $\alpha = 2$ (advective). (b) Mean square displacement at dimensionless time $\dot{\gamma}\Delta t = 1000$ of type-A (red squares) and type-B (blue circles) capsules. Dashed line shows the average value of type B. (c) Scaling of the MSD curves for type-A (red squares) and type-B (blue circles) capsules. Note that the MSDs are normalized by a_A^2 .

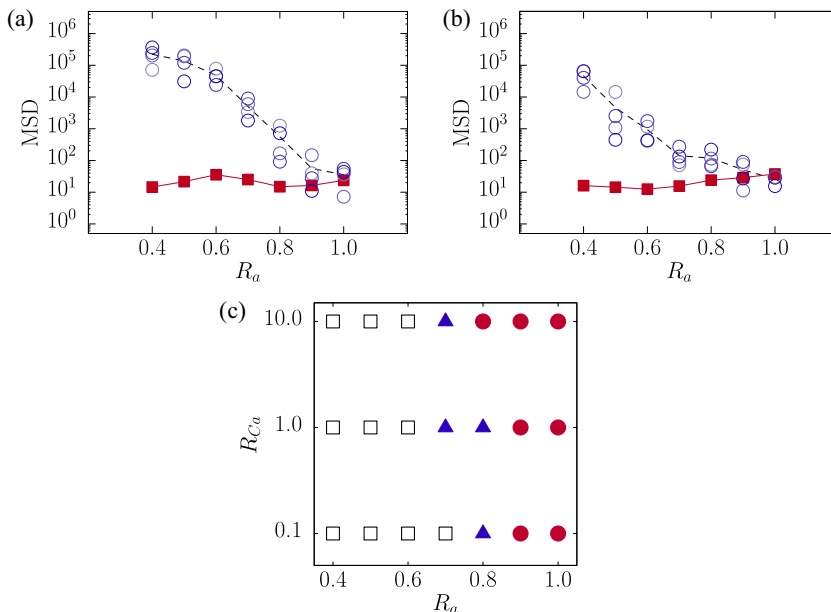


FIG. 5. (a, b) Mean square displacements (MSDs) at dimensionless time $\dot{\gamma}\Delta t = 1000$ of the type-A (red square) and type-B (blue circle) capsules for (a) $R_{Ca} = 0.1$ and (b) $R_{Ca} = 10$. Dashed lines show the average value of the type-B capsules. Note that the MSDs are normalized by a_A^2 . (c) Phase diagram of trapping phenomenon: trapping (circles), segregation (squares), and transition (triangles).

and scaled with $\propto t$ [Figs. 4(a) and 4(c)], thus suggesting the diffusive motion. The scaling factor α in Fig. 4(c) is obtained by fitting the MSD curves (time window: $\dot{\gamma}\Delta t = 10^1 - 10^2$) with a power-law curve, i.e., $\text{MSD} = Dt^\alpha$, where D is the other fitting parameter. Although the crystals of the type-A capsules were more stable with less movement than the type-B capsules, they exhibited diffusive motion, as they changed network topology and remodeled time by time due to the disorders generated by the type-B capsules (see Movie 2 [33]). In contrast, the MSD of the type-B capsules was dependent on R_a . When $R_a = 1.0$ [Fig. 3(a)], the MSD of the type-B capsules was similar to that of the type-A capsules, and both types exhibited diffusive motion, where $\text{MSD} \propto t$. When R_a decreased, the MSD of the type-B capsules increased [Figs. 4(a) and 4(b)], and the difference between the MSDs of the type-A and -B capsules reached several orders of magnitude. The motion of the type-B capsules shifted from the diffusive motion $\alpha \sim 1$ to the advective and superdiffusive motions $\alpha \sim 1.5-2.0$ for $R_a = 0.4$. These results suggest that the capsule crystals can be utilized to segregate capsules of different sizes. In particular, the capsules of comparable sizes are trapped by the crystal structures, whereas smaller capsules are excluded and continuously travel outside the crystal.

Furthermore, the crystal formation of type-A capsules is essential for effective segregation. As shown in Appendix B, there was no drastic MSD difference if the channel width was large ($H/a_A = 8$) as the type-A capsules did not form the crystals.

C. Effect of the stiffness of small capsules

We investigated the influence of the stiffness of small capsules (R_{Ca}) on the segregation phenomenon. Figures 5(a) and 5(b) present the MSD for $R_{Ca} = 10^{-1}$ (type-B capsules were stiffer than type-A capsules by a factor of 10) and $R_{Ca} = 10$ (type-A capsules were stiffer than type-B capsules by a factor of 10), respectively. Although the relative capillary numbers differed by two orders of

magnitude, the fundamental MSD characteristics were the same: diffusive motion for $R_a = 1.0$, and advective motion for $R_a = 0.4$.

Finally, we summarized the segregation phenomenon using the phase diagram shown in Fig. 5(c). The phase diagram reveals that the stiffness of small capsules has only a slight influence, and the size ratio R_a is the main factor determining whether different types of capsules are segregated. This is because, as hypothesized from the theoretical framework, the lift velocity is significantly dependent on the capsule size $u^{\text{lift}} \propto (a/H)^{-3}$.

IV. CONCLUSION

This study reports that the crystal structure of deformable particles can be utilized for particle segregation. As previously reported [16], a group of deformable particles forms a crystal-like structure when subject to a wall-bounded shear flow. In this study, we added several small capsules to a system in which large capsules formed the crystal structure. We observed that the movement of small capsules significantly changed with respect to their radii R_a . In particular, the small capsules exhibited various behaviors from diffusive to superdiffusive motions. Small capsules were trapped in the crystal structure when their radii were nearly the same as the large capsules ($R_a \sim 1$). In particular, they composed the crystal with the large capsules and traveled diffusively. When the size difference was significant ($R_a \leq 0.6$), small capsules were depleted from the crystal layer and continuously traveled outside the crystal layer in an advective manner. Moreover, based on the theory, we revealed that the small capsules were depleted from the crystal structure for $R_a \leq 0.6$ due to their low lift velocities. Due to the rapid decrease in the lift velocity with a decrease in the capsule size, the small capsules are likely to be carried away with the background shear instead of realizing stable capsule-capsule interparticle distances. The large capsules rarely move from the initial position. In contrast, the small capsules are continuously advected and washed away downstream. There would be a drastic difference in MSDs, and our system can be utilized to segregate deformable particles of different sizes. Moreover, the stiffness of the small capsules had a slight influence on this phenomenon.

The findings of the study suggest that the crystal structure of large capsules can be utilized to trap capsules of comparable sizes or exclude small capsules. Although the simulation in this study is limited to capsules with no viscosity ratio, the current strategy is still applicable to capsules with viscosity contrast as biological cells, since the viscosity ratio would only modify the migration velocity [34] and the nature remains the same. This segregation phenomenon is practical for particle sorting applications in microfluidic devices, e.g., extracting rare cells such as platelets smaller than erythrocytes.

ACKNOWLEDGMENTS

This work was supported by JSPS (Japan Society for the Promotion of Science) KAKENHI Grants No. 20K14649 and No. 19K20672 and JST (Japan Science and Technology Agency) ACT-X Grant No. JPMJAX190S, Japan and Multidisciplinary Research Laboratory System for Future Developments (MIRAI LAB). A part of the computation was carried out using the computer resource offered under the category of General Project by the Research Institute for Information Technology, Kyushu University. This work was supported by the MEXT Promotion of Distinctive Joint Research Center Program Grant No. JPMXP0620335886.

APPENDIX A: VALIDATION: GRID SIZE

To verify whether the grid size used in the main text ($\Delta x = a_A/16$) is sufficiently small, we performed simulations with a smaller grid size $\Delta x = a_A/24$ and compare the MSDs in Fig. 6. The simulations with two resolutions both have $\sim 10^4$ differences in MSDs for two capsule types, and there are no qualitative differences in the capsule motions.

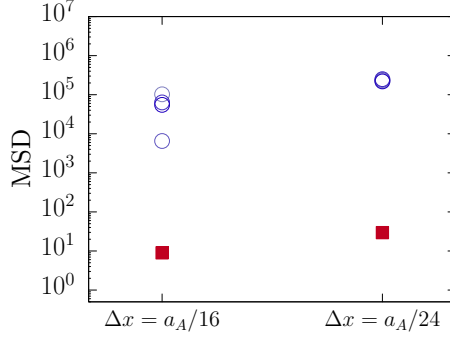


FIG. 6. Mean squared displacements at $\dot{\gamma}\Delta t = 1000$ of two capsule types (red: type-A capsules, blue: type-B capsules) for two grid sizes $\Delta x = a_A/16$ and $a_A/24$. The simulation conditions are $R_{Ca} = 1.0$ and $R_d = 0.4$. Note that the MSDs are normalized by a_A^2 .

APPENDIX B: EFFECT OF CHANNEL WIDTH

Figure 7 compares the MSDs of two capsule types under different channel widths, $H/a_A = 3$ and 8. For narrow channel [$H/a_A = 3$; Figs. 7(a) and 7(c)], type-A capsules have a sharp peak at the channel center, whereas type-B capsules locate in a broader range. As explained in the main text, type-A capsules locate at the channel center most of the time and form the crystal structure in this condition. For the wide channel [$H/a_A = 8$; Figs. 7(b) and 7(d)], the distribution of type-A capsules again occupies the central region of the channel; this has been reported in a previous study of the bimodal capsule suspensions [35]. The distribution of the two capsule types colocalizes in a wider range compared to the narrow channel.

This difference in the distributions leads to a contrast in the traveled distance as shown in Fig. 7(e): there is a slight difference in MSD between the two capsule types for the wide channel, whereas the difference is on the order of $\text{MSD} = 10^3\text{--}10^4$ for the narrow channel. From this analysis, it can be concluded that the narrow channel is suitable for realizing the significant MSD difference between the two capsule types.

APPENDIX C: STABILITY ANALYSIS

We extend the discussion in Sec. III A without assuming that the two capsules locate at an equal distance from the channel center. Let the position of capsules A and B be (x_A, z_A) and (x_B, z_B) , respectively ($x_A < x_B$). The x -directional velocities of capsules due to the quadrupole flow field generated by the other capsule are given as follows:

$$u_x^{A,Q} \sim -\frac{\Sigma_B H}{\mu \ell_x^3} \sim -\frac{\dot{\gamma} a_B^3 H}{\ell_x^3}, \quad (\text{C1})$$

$$u_x^{B,Q} \sim \frac{\Sigma_A H}{\mu \ell_x^3} \sim -\frac{\dot{\gamma} a_A^3 H}{\ell_x^3}, \quad (\text{C2})$$

where $\ell_x = |x_B - x_A|$ is the x distance of capsules, H is the height of the channel, and $\Sigma_A = -\mu \dot{\gamma} a_A^3$ and $\Sigma_B = -\mu \dot{\gamma} a_B^3$ are variables that have the same dimension as the stresslet. The contributions of the background shear flow are given as follows:

$$u_x^{A,SSF} = \dot{\gamma} z_A, \quad (\text{C3})$$

$$u_x^{B,SSF} = \dot{\gamma} z_B. \quad (\text{C4})$$

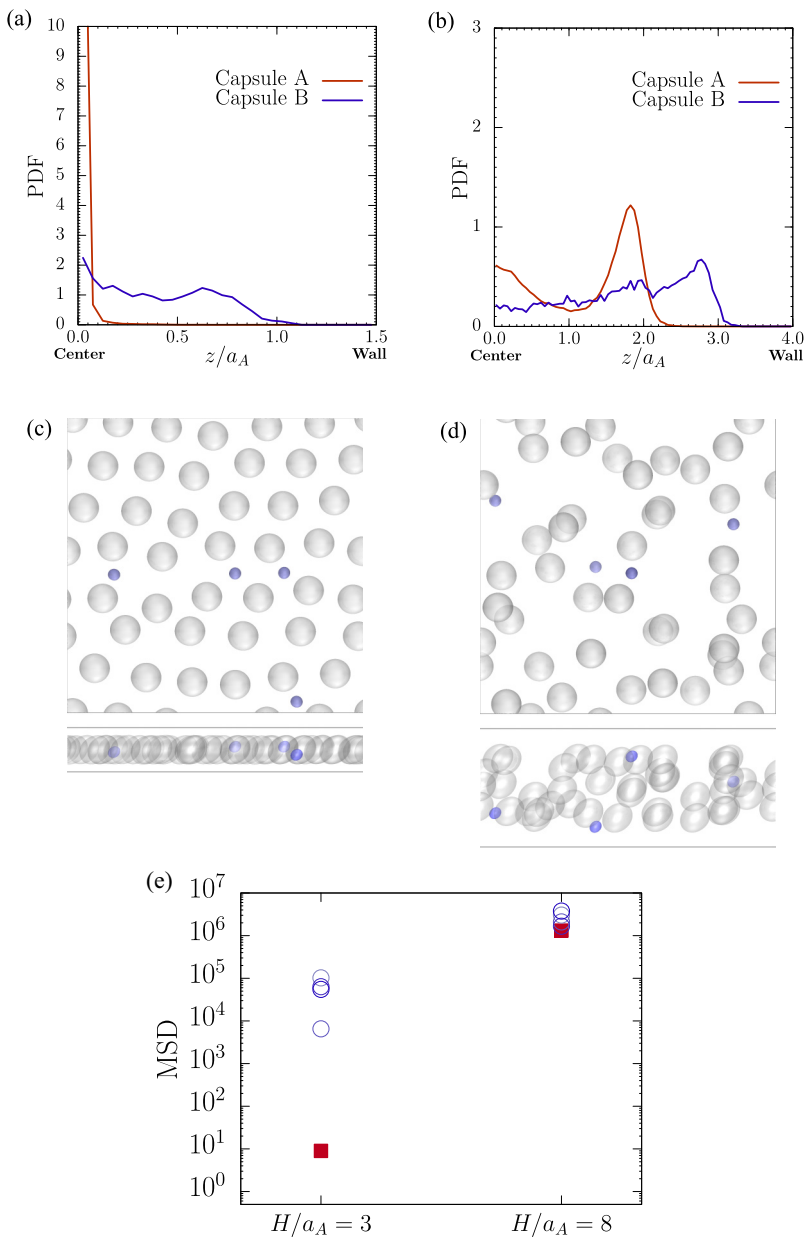


FIG. 7. (a, c) Probability density functions (a) and corresponding snapshot (c) of the two capsule types under $H/a_A = 3$. (b, d) Probability density functions (b) and corresponding snapshot (d) of the two capsule types under $H/a_A = 8$. (e) Mean squared displacements at dimensionless time $\dot{\gamma}\Delta t = 1000$ of the two capsule types (red: type-A capsules, blue: type-B capsules) under different channel widths, $H/a_A = 3$ and $H/a_A = 8$. Note that the MSDs are normalized by a_A^2 . The simulation conditions are $R_{Ca} = 1.0$ and $R_a = 0.4$. The number of capsules is the same for the two channel widths.

The net x -directional velocities are then written as

$$\frac{u_x^A}{\dot{\gamma}a_A} = \frac{u_x^{A,Q} + u_x^{A,SSF}}{\dot{\gamma}a_A} = C_1^A R_a^3 \left(\frac{a_A}{\ell_x}\right)^3 \frac{H}{a_A} + \frac{z_A}{a_A}, \quad (\text{C5})$$

$$\frac{u_x^B}{\dot{\gamma}a_A} = \frac{u_x^{B,Q} + u_x^{B,SSF}}{\dot{\gamma}a_A} = -C_1^B \left(\frac{a_A}{\ell_x}\right)^3 \frac{H}{a_A} + \frac{z_B}{a_A}, \quad (\text{C6})$$

where $R_a = a_B/a_A$ is the size ratio, and C_1^A and C_1^B are the numerical prefactors of $O(1)$. The relative x velocity of capsule B against capsule A is

$$\frac{U_x^{AB}}{\dot{\gamma}a_A} = \frac{u_x^B - u_x^A}{\dot{\gamma}a_A} = -\frac{H}{a_A} \left(\frac{a_A}{\ell_x}\right)^3 (C_1^A R_a^3 + C_1^B) + \frac{z_B - z_A}{a_A}. \quad (\text{C7})$$

The wall-induced lift velocities are given as [19]

$$u_z^{A,\text{lift}} \sim \frac{\Sigma_A z_A}{\mu H^3} \sim -\frac{\dot{\gamma} a_A^3 z_A}{H^3}, \quad (\text{C8})$$

$$u_z^{B,\text{lift}} \sim \frac{\Sigma_B z_B}{\mu H^3} \sim -\frac{\dot{\gamma} a_B^3 z_B}{H^3}, \quad (\text{C9})$$

and the z -directional velocities due to the hydrodynamic quadrupolar interactions are given as follows:

$$u_z^{A,Q} \sim \frac{\Sigma_B}{\mu H^2} \sqrt{\frac{\ell_x}{H}} \exp\left(-\frac{b_2 \ell_x}{H}\right) \cos\left(\frac{b_1 \ell_x}{H} - b_3\right), \quad (\text{C10})$$

$$u_z^{B,Q} \sim -\frac{\Sigma_A}{\mu H^2} \sqrt{\frac{\ell_x}{H}} \exp\left(-\frac{b_2 \ell_x}{H}\right) \cos\left(\frac{b_1 \ell_x}{H} - b_3\right), \quad (\text{C11})$$

where $b_1 \sim 2.25$, $b_2 \sim 4.21$, and $b_3 \sim 2.49$ [16]. The net z -directional velocities are written as

$$\frac{u_z^A}{\dot{\gamma}a_A} = \frac{u_z^{A,Q} + u_z^{A,\text{lift}}}{\dot{\gamma}a_A} = \left(\frac{a_A}{H}\right)^3 \left[-C_3^A \frac{z_A}{a_A} - C_2^A R_a^3 \frac{H}{a_A} \sqrt{\frac{\ell_x}{H}} \exp\left(-\frac{b_2 \ell_x}{H}\right) \cos\left(\frac{b_1 \ell_x}{H} - b_3\right) \right], \quad (\text{C12})$$

$$\frac{u_z^B}{\dot{\gamma}a_A} = \frac{u_z^{B,Q} + u_z^{B,\text{lift}}}{\dot{\gamma}a_A} = \left(\frac{a_A}{H}\right)^3 \left[-C_3^B R_a^3 \frac{z_B}{a_A} + C_2^B \frac{H}{a_A} \sqrt{\frac{\ell_x}{H}} \exp\left(-\frac{b_2 \ell_x}{H}\right) \cos\left(\frac{b_1 \ell_x}{H} - b_3\right) \right]. \quad (\text{C13})$$

Equations (C7), (C12), and (C13) have a stable fixed point: $(U_x^{AB}, u_z^A, u_z^B) = (0, 0, 0)$ at $(\ell_x^0/a_A, z_A^0/a_A, z_B^0/a_A) \sim (5.5, 0, 0)$ when $H/a_A = 3.0$.

Here we consider a small perturbation $(\delta x, \delta z_A, \delta z_B)$ around the stable fixed point. Using the Taylor series expansion

$$\left(\frac{a_A}{\ell_x^0 + \delta x}\right)^3 = \left(\frac{a_A}{\ell_x^0}\right)^3 - 3\left(\frac{a_A}{\ell_x^0}\right)^4 \frac{\delta x}{a_A} + O(\delta x^2), \quad (\text{C14})$$

$$\sqrt{\frac{\ell_x^0 + \delta x}{H}} = \sqrt{\frac{\ell_x^0}{H}} + \frac{1}{2} \sqrt{\frac{a_A^2}{\ell_x^0 H}} \frac{\delta x}{a_A} + O(\delta x^2), \quad (\text{C15})$$

$$\exp\left[-\frac{b_2(\ell_x^0 + \delta x)}{H}\right] = \exp\left(-\frac{b_2 \ell_x^0}{H}\right) - \frac{b_2 a_A}{H} \exp\left(-\frac{b_3 \ell_x^0}{H}\right) \frac{\delta x}{a_A} + O(\delta x^2), \quad (\text{C16})$$

$$\cos\left[\frac{b_1(\ell_x^0 + \delta x)}{H} - b_3\right] = \cos\left(\frac{b_1 \ell_x^0}{H} - b_3\right) - \frac{b_1 a_A}{H} \sin\left(\frac{b_1 \ell_x^0}{H} - b_3\right) \frac{\delta x}{a_A} + O(\delta x^2), \quad (\text{C17})$$

and neglecting the second-order term, we obtain the following linearized equations:

$$\begin{aligned} \frac{\delta U_x^{AB}}{\dot{\gamma} a_A} &= -\frac{H}{a_A} \left[\frac{a_A}{(\ell_x^0 + \delta x)} \right]^3 (C_1^A R_a^3 + C_1^B) + \frac{(z_B^0 + \delta z_B) - (z_A^0 + \delta z_A)}{a_A} \\ &\sim 3 \frac{H}{a_A} \left(\frac{a_A}{\ell_x^0} \right)^4 \frac{\delta x}{a_A} (C_1^A R_a^3 + C_1^B) + \frac{\delta z_B - \delta z_A}{a_A}, \end{aligned} \quad (\text{C18})$$

$$\begin{aligned} \frac{\delta u_z^A}{\dot{\gamma} a_A} &= \left(\frac{a_A}{H} \right)^3 \left\{ -C_3^A \frac{(z_A^0 + \delta z_A)}{a_A} - C_2^A R_a^3 \frac{H}{a_A} \sqrt{\frac{(\ell_x^0 + \delta x)}{H}} \right. \\ &\quad \times \exp \left[-\frac{b_2(\ell_x^0 + \delta x)}{H} \right] \cos \left[\frac{b_1(\ell_x^0 + \delta x)}{H} - b_3 \right] \left. \right\} \\ &\sim -C_3^A \left(\frac{a_A}{H} \right)^3 \frac{\delta z_A}{a_A} - C_2^A R_a^3 \left(\frac{a_A}{H} \right)^2 \left[-\sqrt{\frac{\ell_x^0}{H}} \exp \left(-\frac{b_2 \ell_x^0}{H} \right) \frac{b_1 a_A}{H} \sin \left(\frac{b_1 \ell_x^0}{H} - b_3 \right) \right. \\ &\quad \left. - \sqrt{\frac{\ell_x^0}{H}} \frac{b_2 a_A}{H} \exp \left(-\frac{b_2 \ell_x^0}{H} \right) \cos \left(\frac{b_1 \ell_x^0}{H} - b_3 \right) \right. \\ &\quad \left. + \frac{1}{2} \sqrt{\frac{a_A^2}{\ell_x^0 H}} \exp \left(-\frac{b_2 \ell_x^0}{H} \right) \cos \left(\frac{b_1 \ell_x^0}{H} - b_3 \right) \right] \frac{\delta x}{a_A}, \end{aligned} \quad (\text{C19})$$

$$\begin{aligned} \frac{\delta u_z^B}{\dot{\gamma} a_A} &= \left(\frac{a_A}{H} \right)^3 \left\{ -C_3^B R_a^3 \frac{(z_B^0 + \delta z_B)}{a_A} + C_2^B \frac{H}{a_A} \sqrt{\frac{(\ell_x^0 + \delta x)}{H}} \right. \\ &\quad \times \exp \left[-\frac{b_2(\ell_x^0 + \delta x)}{H} \right] \cos \left[\frac{b_1(\ell_x^0 + \delta x)}{H} - b_3 \right] \left. \right\} \\ &\sim -C_3^B \left(\frac{a_A}{H} \right)^3 R_a^3 \frac{\delta z_B}{a_A} + C_2^B \left(\frac{a_A}{H} \right)^2 \left[-\sqrt{\frac{\ell_x^0}{H}} \exp \left(-\frac{b_2 \ell_x^0}{H} \right) \frac{b_1 a_A}{H} \sin \left(\frac{b_1 \ell_x^0}{H} - b_3 \right) \right. \\ &\quad \left. - \sqrt{\frac{\ell_x^0}{H}} \frac{b_2 a_A}{H} \exp \left(-\frac{b_2 \ell_x^0}{H} \right) \cos \left(\frac{b_1 \ell_x^0}{H} - b_3 \right) \right. \\ &\quad \left. + \frac{1}{2} \sqrt{\frac{a_A^2}{\ell_x^0 H}} \exp \left(-\frac{b_2 \ell_x^0}{H} \right) \cos \left(\frac{b_1 \ell_x^0}{H} - b_3 \right) \right] \frac{\delta x}{a_A}, \end{aligned} \quad (\text{C20})$$

Equations (C18), (C19), and (C20) can be written in matrix form as follows:

$$\begin{pmatrix} \delta U_x^{AB} / \dot{\gamma} a_A \\ \delta u_z^A / \dot{\gamma} a_A \\ \delta u_z^B / \dot{\gamma} a_A \end{pmatrix} = \mathbf{M} \begin{pmatrix} \delta x / a_A \\ \delta z_A / a_A \\ \delta z_B / a_A \end{pmatrix}, \quad (\text{C21})$$

and the components of the coefficient matrix \mathbf{M} are

$$\begin{aligned} M_{11} &= 3 \frac{H}{a_A} \left(\frac{a_A}{\ell_x^0} \right)^4 \{ C_1^A R_a^3 + C_1^B \}, \\ M_{12} &= -1, \\ M_{13} &= 1, \\ M_{21} &= -C_2^A \left(\frac{a_A}{H} \right)^2 R_a^3 S, \end{aligned}$$

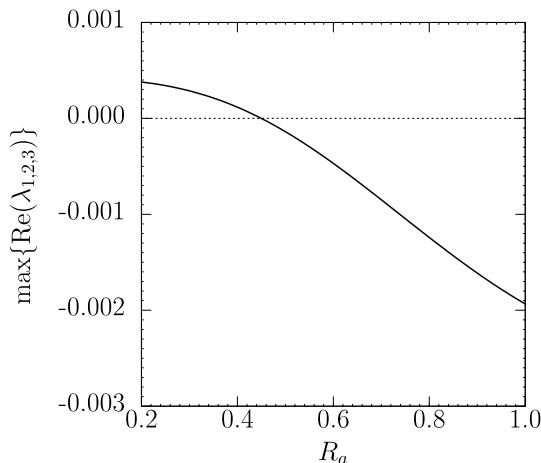


FIG. 8. Maximal value of real part of the eigenvalues of \mathbf{M} with prefactors $C_1^A = C_1^B = 0.08$, $C_2^A = C_2^B = 15$, $C_3^A = C_3^B = 1.5$, and $H/a_A = 3.0$ are utilized.

$$\begin{aligned}
 M_{22} &= -C_3^A \left(\frac{a_A}{H}\right)^3, \\
 M_{23} &= 0, \\
 M_{31} &= C_2^B \left(\frac{a_A}{H}\right)^2 S, \\
 M_{32} &= 0, \\
 M_{33} &= -C_3^B \left(\frac{a_A}{H}\right)^3 R_a^3,
 \end{aligned} \tag{C22}$$

$$\begin{aligned}
 S &= -\sqrt{\frac{\ell_x^0}{H}} \exp\left(-\frac{b_2 \ell_x^0}{H}\right) \frac{b_1 a_A}{H} \sin\left(\frac{b_1 \ell_x^0}{H} - b_3\right) \\
 &\quad -\sqrt{\frac{\ell_x^0}{H}} \frac{b_2 a_A}{H} \exp\left(-\frac{b_2 \ell_x^0}{H}\right) \cos\left(\frac{b_1 \ell_x^0}{H} - b_3\right) \\
 &\quad + \frac{1}{2} \sqrt{\frac{a_A^2}{\ell_x^0 H}} \exp\left(-\frac{b_2 \ell_x^0}{H}\right) \cos\left(\frac{b_1 \ell_x^0}{H} - b_3\right).
 \end{aligned} \tag{C23}$$

The matrix \mathbf{M} has three eigenvalues $\lambda_1, \lambda_2, \lambda_3$. The real parts of $\{\lambda_{1,2,3}\}$ characterize the stability of this system. The system is stable if all real parts of $\{\lambda_{1,2,3}\}$ are negative. Figure 8 shows the maximal value of the real part of $\{\lambda_{1,2,3}\}$ as a function of R_a with $H/a_A = 3.0$. Note that the numerical prefactors are estimated as $C_1^A = C_1^B = 0.08$, $C_2^A = C_2^B = 15$, $C_3^A = C_3^B = 1.5$ by fitting the capsule trajectories of a 3D simulation under $Ca = 0.1$ and $R_a = 1$. The stability of the two-capsule system decreases with a decrease of R_a and becomes unstable (eigenvalues have positive real parts) around $R_a \sim 0.45$. The criteria may differ in the many-capsule system; small capsules may find it more difficult to reach (or stay at) the stable point due to the complex interaction between capsules.

[1] D. R. Gossett, W. M. Weaver, A. J. Mach, S. C. Hur, H. T. K. Tse, W. Lee, H. Amini, and D. Di Carlo, Label-free cell separation and sorting in microfluidic systems, *Anal. Bioanal. Chem.* **397**, 3249 (2010).

- [2] D. Di Carlo, D. Irimia, R. G. Tompkins, and M. Toner, Continuous inertial focusing, ordering, and separation of particles in microchannels, *Proc. Natl. Acad. Sci. USA* **104**, 18892 (2007).
- [3] M. Masaeli, E. Sollier, H. Amini, W. Mao, K. Camacho, N. Doshi, S. Mitragotri, A. Alexeev, and D. Di Carlo, Continuous Inertial Focusing and Separation of Particles by Shape, *Phys. Rev. X* **2**, 031017 (2012).
- [4] J. Zhang, S. Yan, D. Yuan, G. Alici, N.-T. Nguyen, M. E. Warkiani, and W. Li, Fundamentals and applications of inertial microfluidics: A review, *Lab Chip* **16**, 10 (2016).
- [5] D. Di Carlo, Inertial microfluidics, *Lab Chip* **9**, 3038 (2009).
- [6] N. Nivedita, P. Ligrani, and I. Papautsky, Dean flow dynamics in low-aspect ratio spiral microchannels, *Sci. Rep.* **7**, 44072 (2017).
- [7] D. Matsunaga, F. Meng, A. Zöttl, R. Golestanian, and J. M. Yeomans, Focusing and Sorting of Ellipsoidal Magnetic Particles in Microchannels, *Phys. Rev. Lett.* **119**, 198002 (2017).
- [8] D. Matsunaga, A. Zöttl, F. Meng, R. Golestanian, and J. M. Yeomans, Far-field theory for trajectories of magnetic ellipsoids in rectangular and circular channels, *IMA J. Appl. Math.* **83**, 767 (2018).
- [9] A. A. S. Bhagat, H. W. Hou, L. D. Li, C. T. Lim, and J. Han, Pinched flow coupled shear-modulated inertial microfluidics for high-throughput rare blood cell separation, *Lab Chip* **11**, 1870 (2011).
- [10] J. Zhou and I. Papautsky, Size-dependent enrichment of leukocytes from undiluted whole blood using shear-induced diffusion, *Lab Chip* **19**, 3416 (2019).
- [11] W. Uijttewaai, E. Nijhof, P. Bronkhorst, E. Den Hartog, and R. M. Heethaar, Near-wall excess of platelets induced by lateral migration of erythrocytes in flowing blood, *Am. J. Physiol. Heart Circ. Physiol.* **264**, H1239 (1993).
- [12] J. Nam, H. Lim, D. Kim, H. Jung, and S. Shin, Continuous separation of microparticles in a microfluidic channel via the elasto-inertial effect of non-Newtonian fluid, *Lab Chip* **12**, 1347 (2012).
- [13] T. Tanaka, T. Ishikawa, K. Numayama-Tsuruta, Y. Imai, H. Ueno, N. Matsuki, and T. Yamaguchi, Separation of cancer cells from a red blood cell suspension using inertial force, *Lab Chip* **12**, 4336 (2012).
- [14] T. Tanaka, T. Ishikawa, K. Numayama-Tsuruta, Y. Imai, H. Ueno, T. Yoshimoto, N. Matsuki, and T. Yamaguchi, Inertial migration of cancer cells in blood flow in microchannels, *Biomed. Microdevices* **14**, 25 (2012).
- [15] M. G. Lee, J. H. Shin, C. Y. Bae, S. Choi, and J.-K. Park, Label-free cancer cell separation from human whole blood using inertial microfluidics at low shear stress, *Anal. Chem.* **85**, 6213 (2013).
- [16] Z. Shen, T. M. Fischer, A. Farutin, P. M. Vlahovska, J. Harting, and C. Misbah, Blood Crystal: Emergent Order of Red Blood Cells under Wall-Confined Shear Flow, *Phys. Rev. Lett.* **120**, 268102 (2018).
- [17] K. B. Migler, String Formation in Sheared Polymer Blends: Coalescence, Breakup, and Finite Size Effects, *Phys. Rev. Lett.* **86**, 1023 (2001).
- [18] S. Singha, A. R. Malipeddi, M. Zurita-Gotor, K. Sarkar, K. Shen, M. Loewenberg, K. B. Migler, and J. Blawdziewicz, Mechanisms of spontaneous chain formation and subsequent microstructural evolution in shear-driven strongly confined drop monolayers, *Soft Matter* **15**, 4873 (2019).
- [19] J. R. Smart and D. T. Leighton Jr, Measurement of the drift of a droplet due to the presence of a plane, *Phys. Fluids* **3**, 21 (1991).
- [20] S. Nix, Y. Imai, D. Matsunaga, T. Yamaguchi, and T. Ishikawa, Lateral migration of a spherical capsule near a plane wall in stokes flow, *Phys. Rev. E* **90**, 043009 (2014).
- [21] H. Ito, D. Matsunaga, and Y. Imai, Shear viscosity of bimodal capsule suspensions in simple shear flow, *Phys. Rev. Fluids* **4**, 113601 (2019).
- [22] R. Skalak, A. Tozeren, R. Zarda, and S. Chien, Strain energy function of red blood cell membranes, *Biophys. J.* **13**, 245 (1973).
- [23] J. Walter, A.-V. Salsac, D. Barthès-Biesel, and P. Le Tallec, Coupling of finite element and boundary integral methods for a capsule in a stokes flow, *Int. J. Numer. Meth. Eng.* **83**, 829 (2010).
- [24] X. Li and K. Sarkar, Effects of inertia on the rheology of a dilute emulsion of drops in shear, *J. Rheol.* **49**, 1377 (2005).
- [25] S. Chen and G. D. Doolen, Lattice Boltzmann method for fluid flows, *Annu. Rev. Fluid Mech.* **30**, 329 (1998).
- [26] T. Krüger, H. Kusumaatmaja, A. Kuzmin, O. Shardt, G. Silva, and E. M. Viggen, *The Lattice Boltzmann Method* (Springer International Publishing, Cham, 2017).

- [27] C. S. Peskin, The immersed boundary method, *Acta Numerica* **11**, 479 (2002).
- [28] J. B. Freund, Leukocyte margination in a model microvessel, *Phys. Fluids* **19**, 023301 (2007).
- [29] N. Takeishi, Y. Imai, K. Nakaaki, T. Yamaguchi, and T. Ishikawa, Leukocyte margination at arteriole shear rate, *Physiol. Rep.* **2**, e12037 (2014).
- [30] N. Takeishi, Y. Imai, T. Yamaguchi, and T. Ishikawa, Flow of a circulating tumor cell and red blood cells in microvessels, *Phys. Rev. E* **92**, 063011 (2015).
- [31] N. Takeishi, Y. Imai, S. Ishida, T. Omori, R. D. Kamm, and T. Ishikawa, Cell adhesion during bullet motion in capillaries, *Am. J. Physiol. Heart Circ. Physiol.* **311**, H395 (2016).
- [32] S. Ishida, A. Ami, and Y. Imai, Factors diminishing cytoadhesion of red blood cells infected by *Plasmodium falciparum* in arterioles, *Biophys. J.* **113**, 1163 (2017).
- [33] See Supplemental Material at <http://link.aps.org/supplemental/10.1103/PhysRevFluids.7.063601> for movies showing capsule movements.
- [34] S. Nix, Y. Imai, and T. Ishikawa, Lateral migration of a capsule in a parabolic flow, *J. Biomech.* **49**, 2249 (2016).
- [35] A. Kumar, R. G. H. Rivera, and M. D. Graham, Flow-induced segregation in confined multicomponent suspensions: Effects of particle size and rigidity, *J. Fluid Mech.* **738**, 423 (2014).